



Effect of buoyancy on the radiative extinction limit of low-strain-rate nonpremixed methane–air flames

Anthony Hamins^a, Matthew Bundy^a, Chang Bo Oh^{b,*}, Sung Chan Kim^{a,1}

^a National Institute of Standards and Technology, Gaithersburg, MD 20899-8663, USA

^b Division of Safety Engineering, Pukyong National University, Busan 608-739, Republic of Korea

Received 24 October 2006; received in revised form 20 April 2007; accepted 24 May 2007

Available online 15 August 2007

Abstract

The structure and extinction of nonpremixed flames were investigated through comparison of experiments and calculations using a counterflow configuration. Experiments were conducted at the NASA Glenn Research Center's 2.2-s drop tower to attain suppression and temperature measurements in low-strain nonpremixed methane–air microgravity flames. Suppression measurements using nitrogen added to the fuel stream were performed for global strain rates from 7 to 50 s⁻¹. Judicious hardware selection and an optimized experimental procedure facilitated rapid, controllable, and repeatable flame extinction measurements. The minimum nitrogen volume fraction in the fuel stream needed to ensure suppression for all strain rates in microgravity was measured to be 0.855 ± 0.016, associated with the turning point, which occurred at a global strain rate of 15 s⁻¹. This value was higher than the analogous value in normal gravity. Flame temperature measurements were attained in the high-temperature region of the flame ($T > 1200$ K) using visible emission from a SiC filament positioned axially along the burner centerline. The suppression and temperature measurements were used to validate a two-dimensional flame simulation developed here, which included buoyancy effects and finite-rate kinetics. The simulations yielded insight into the differences between microgravity and normal gravity suppression results and also explained the inadequacy of the one-dimensional model results to explain the microgravity suppression results.

Published by Elsevier Inc. on behalf of The Combustion Institute.

Keywords: Extinction; Flame structure; Microgravity; Nonpremixed

1. Introduction

Unwanted fires typically occur due to nonpremixed combustion. The agent concentration required to achieve the suppression (or extinction) of nonpremixed flames is an important consideration for de-

sign of fire protection systems, as engineers rely on suppression data to estimate suppressant mass requirements for total flooding applications. Information regarding critical suppressant concentrations in the high-strain-rate regime is less important than in the low-strain-rate regime, because low-strain-rate conditions typically require higher agent concentrations, and fire protection design must be based on worst-case conditions. The initial stage of an unwanted fire in a microgravity environment, such as an orbiting space platform, will likely occur at a low

* Corresponding author. Fax: +82 51 620 1516.

E-mail address: turboh@hanmail.net (C.B. Oh).

¹ Current address: School of Mechanical Engineering, Chung Ang University, Seoul 155-756, Republic of Korea.

strain rate. The actual value of the strain rate will depend on the combustion configuration and local environmental conditions such as air currents generated by the fire itself and any forced ventilation.

A review of the literature indicates that there has been little work on low ($<30 \text{ s}^{-1}$)-strain-rate flame suppression by an agent, and practically none on the suppression of low-strain-rate adiabatic flames in microgravity. Related studies include Refs. [1–10]. Maruta et al. [1] conducted the first comprehensive suppression measurements of very-low-strain nonpremixed flames in microgravity using the Japan Microgravity Center (JAMIC) 10-s drop tower. In their study, the suppression of methane–air diffusion flames with N_2 added to the fuel stream was measured under microgravity conditions. The minimum methane concentration required to sustain combustion was measured to decrease as the strain rate decreased until a critical value was observed. As the global strain rate was further reduced, the required methane concentration increased. This behavior was denoted as a “turning point” and was attributed to the enhanced importance of radiative loss in low-strain-rate flames. In terms of fire safety, the turning point agent concentration represents a fundamental limit for nonpremixed flames, ensuring suppression for all flow conditions. Bundy et al. [2] observed similar extinction behavior in low-strain-rate normal-gravity flames. Zhang and Egolfopoulos [3] studied extinction of premixed flames in microgravity using a 2.2-s drop tower. Ronney [4] examined the effect of CF_3Br on the burning velocities, flammability limits, and minimum ignition energies of alkane/air mixtures and determined that flame propagation occurred over a wider range of conditions in normal gravity than in microgravity. Van der Wege et al. [5] reported on the shape and the visual character of methane jets ($\text{Re} = 100$) flowing into a quiescent-agent-laden environment. Other investigators have examined extinction of diffusion flames through conductive losses to walls [6] or transient two-phase diffusion effects in flames burning alcohol fuels [7]. Olsen and T’ien [8] reported on the structure of low-stretch PMMA diffusion flames burning in normal gravity.

Experimental observations under microgravity conditions show that counterflow flames appear to be nearly flat [1]. Under normal gravity conditions, high-strain-rate flames are also flat, as buoyancy is overwhelmed by convection. As the strain rate decreases in normal gravity, buoyancy forces become relatively more important and the flames are clearly curved. One-dimensional flame codes such as OPPDIF [9] are based on a similarity solution that neglects buoyancy. These one-dimensional steady-state simulations fail to describe the multidimensional structure of low-strain-rate normal-gravity flames, nor do they capture

the dynamics of a flame during the transition from normal to microgravity. To gain physical insight, a numerical method is needed that is capable of simulating flames under the influence of buoyancy, and to better understand the effects of finite burner size on the detailed flame structure. Frouzakis et al. [10] developed a two-dimensional (2D) direct numerical simulation that considered potential problems arising from the use of a 1D similarity solution along the flow field centerline to represent the character of 2D counterflow flames [10]. In their study, the structure of low-strain-rate counterflow H_2 –air flames was investigated.

The objective of this study was to investigate the structure and suppression of low-strain-rate counterflow nonpremixed flames in both normal gravity and microgravity through measurements and numerical simulations. The suppression effectiveness of a suppressant (N_2) added to the fuel stream of low-strain-rate methane–air diffusion flames was measured. Flame temperature measurements were attained in the high-temperature region of the flame by radiative emission from a thin filament positioned axially along the burner centerline. A two-dimensional (2D) flame simulation, including buoyancy effects, was developed and was validated with the flame suppression and temperature profile measurements.

As mentioned above, microgravity suppression measurements similar to those reported here were previously conducted [1]. Fig. 1 replots the results presented in Fig. 4 of Ref. [1], which shows a comparison of the previous microgravity measurements with their calculations based on a 1D similarity solution. In this study (and in Fig. 1), the global strain rate (a_g) was defined [11] as

$$a_g = \frac{2V_a}{L} \left(1 + \frac{V_f \sqrt{\rho_f}}{V_a \sqrt{\rho_a}} \right), \quad (1)$$

where the parameters V and ρ denote the mean velocity and density of the reactant streams at the duct boundaries, L is the duct separation distance, and the subscripts a and f represent the air and fuel streams, respectively. The definition of the global strain rate used here is larger than the definition used in Ref. [1] by a factor of 2. While there are similarities in the gross trends between the measurements and the simulation results in Fig. 1, some interesting differences are evident, particularly in the very-low-strain-rate regime, where the calculations overpredict the critical agent concentration in the fuel stream at extinction. The differences between the model and the experimental results could be associated with a number of issues. Reference [1] reports that the location of mesh screens in the exits of the burner ducts was varied for each of the experimental conditions. The location of the mesh screens provides a well-defined boundary

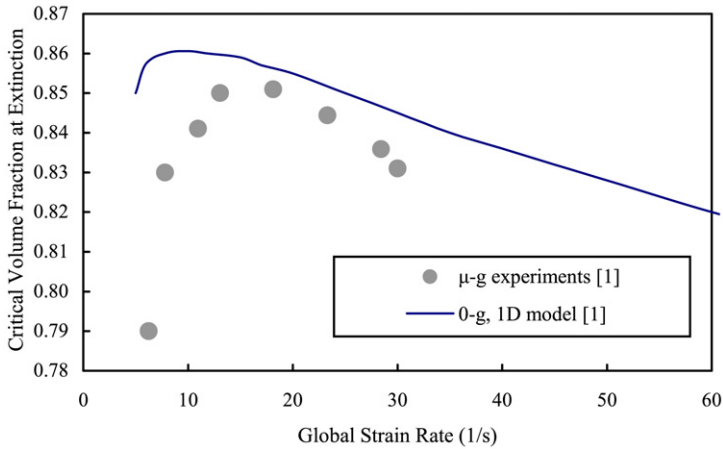


Fig. 1. Previously computed (1D model) and measured critical nitrogen volume fraction in the fuel stream for suppression of CH_4 flames in microgravity [1].

condition on the flow field within the duct, which impacts the flow boundary conditions and possibly the comparison of the suppression results with the model. In addition, the combustion test chamber in Ref. [1] was filled with air, rather than an inert nonreactive gas such as nitrogen. Experiments conducted in normal gravity show that use of an air ambient in the combustion chamber impacts the extinction results [2]. For these reasons, the work reported here revisits the previous microgravity suppression measurements. In addition, this study extends the previous experimental work by investigating the detailed flame structure of the near extinction flames through measurements of the local temperature. This information was useful for validation of a 2D numerical code developed here and subsequently used to investigate the mechanisms of flame extinction under normal and microgravity conditions.

Like the measurements, there are also a number of questions related to the application of the 1D similarity model to the previous experimental measurements [1]. At low strain rates, the flames were rather thick, and the flame diameter/flame thickness ratio was not very large. Only when this ratio is large enough can the flame be classified as one-dimensional. In this case [1], lateral heat and diffusion losses may be significant, and neglect of these terms through use of a 1D similarity model may be problematic. The 2D model developed here attempts to address these issues.

Han et al. [12] recently reported on the structure of ultra-low-stretch ($\sim 2 \text{ s}^{-1}$) methane nonpremixed flames. Their study considered radiation effects and extinction in curved flames established in normal gravity by flowing diluted fuel in a downward direction through a porous spherically symmetric burner with a large radius of curvature. Heat losses to the

burner were characterized and the computational results were found to be consistent with experimental observations.

In this study, conductive heat losses to the burner were avoided, which impacted the range of strain rates investigated, because flame thickness increases as the strain rate decreases. Here, the global strain rate (a_g) was varied from 7 to 50 s^{-1} in microgravity flames and from 14 to 50 s^{-1} in normal gravity flames to avoid conductive heat losses to the burner—as determined through consideration of the profile of temperature near the burner boundaries. To maximize the range of strain rates considered in the normal gravity flames considered here, the approach used by Ref. [2] was applied, in which the velocity ratio of the air stream to the fuel stream (V_a/V_f in Eq. (1)) was adjusted so that the flame location was forced towards the center of the flowfield, away from the burner ducts.

2. Experimental methods

2.1. Experimental apparatus

Microgravity experiments were conducted at the NASA Glenn Research Center 2.2-s drop tower. A 15-mm-diameter stainless steel counterflow burner was enclosed in a 25-L cylindrical chamber. The experimental hardware was mounted in a standard NASA drop rig. A schematic of the burner and flow system is shown in Fig. 2. To control each gas flow (air, CH_4 , and N_2 added to the fuel stream), a pressure transducer, a solenoid valve, a pressure regulator, and a fast-response-time ($\approx 50 \text{ ms}$) pressure controller were placed upstream of a critical flow orifice. The burner was designed to have a minimal dead volume

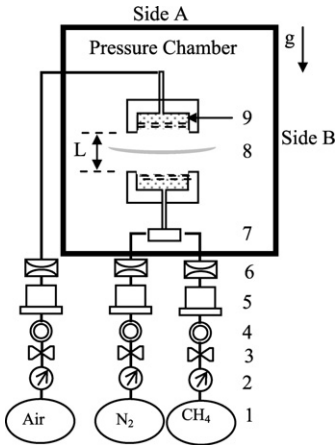


Fig. 2. Schematic of counterflow system including (1) gas cylinders, (2) pressure transducers, (3) solenoid valves, (4) pressure regulators, (5) pressure controllers/sensors, (6) critical flow orifices, (7) mixing tee, (8) burner, and (9) glass beads and metal screens.

as glass beads and a series of fine mesh steel screens were used to impose a near plug-flow velocity profile. The duct separation distance, L , was 15 mm (see Fig. 2) and the wire mesh screens were positioned ≈ 1 mm into each of the ducts. This exact geometry was considered in the 2D numerical model developed here. The reactants were stored in pressurized 500-cm³ stainless steel cylinders. The oxygen content in the bottled air was measured to be $(20.93 \pm 0.04)\%$ using a paramagnetic analyzer [13]. The fuel was research grade methane (99.99% purity). Flow control and data acquisition were performed using a PC104 microprocessor with 320 MB of flash memory and a 16-bit data acquisition board sampling at 200 Hz.

2.2. Suppression measurements

Accurate suppression measurements in 2.2 s of microgravity were attained by judicious hardware selection (50-ms time response pressure transducers, associated critical flow orifices, and a small dead-volume flow system) and development of an optimized experimental procedure in which microgravity conditions were initiated under near-extinction (normal gravity) flame conditions. The combustion chamber was evacuated and filled to 101 kPa with N₂, in contrast to the previous measurements [1]. The flow configuration used for these experiments used air from the top duct and methane diluted with nitrogen from the bottom duct. The initial N₂ volume fraction was set as close to normal gravity suppression conditions as possible. Ignition was accomplished by positioning and energizing a 0.25-mm-diameter (6-cm-long) coiled Pt + 30% Rh wire between the

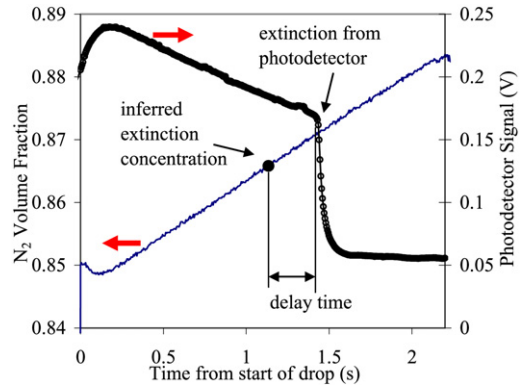


Fig. 3. Measured nitrogen volume fraction in the fuel stream of a 15 s^{-1} methane–air flame as a function of time. The photodetector signal is also shown, indicating the time of flame extinction.

ducts after the reactant flows were initiated. Upon ignition, the ignition wire was simultaneously de-energized and slowly retracted from the flame at a rate of 2 cm/s to minimize convective disturbances. About 5 s later, after the flame had stabilized, microgravity conditions were initiated by releasing the drop package. From this point on, the extinction experiments were automated.

Flame suppression was achieved by increasing the agent flow and simultaneously decreasing the fuel flow, while maintaining a constant global strain rate, until a critical agent volume fraction in the fuel stream was attained. For each experiment, the onboard computer recorded the transient strain rate the nitrogen concentration in the fuel stream, the chamber pressure, the start and end of the drop period, the pressure at state 5 in Fig. 2, and the signal from a photodetector inside the chamber. Acceleration levels during the drop were typically 10^{-4} m/s^2 . The photodetector signal dropped abruptly when the flame was extinguished and the time of suppression was independently confirmed from inspection of a digital video recording. The suppression concentration was inferred by determining the N₂ concentration based on the time of flame suppression and the delay time of the system.

The experimental method is illustrated in Fig. 3, which shows the measured nitrogen volume fraction in the fuel stream of a 15 s^{-1} methane–air flame as a function of time after drop initiation. The photodetector signal is also shown, which indicated the time of flame extinction when its value rapidly decreased. The critical N₂ concentration at extinction was inferred from the concentration–time data through consideration of the system delay time, which was the time of travel from the fuel/N₂ mixing tee (see component number 7 in Fig. 2) to the flame zone, at the

middle of the flow field. The delay time was calculated through consideration of the system volume and the gas flows. The calculation was verified by performing extinction experiments for different N₂ “ramping” rates during the experimental drop for the same flame conditions, with the ramping rates varying about 30%. These experiments resulted in determination of the values of the critical N₂ volume fraction at extinction to within 0.1%, verifying the estimates of the system delay times. Experiments in normal gravity also showed that the critical N₂ suppression volume fraction was independent of the N₂ ramping rate, for the rates considered here. Since the N₂ volume fraction at the beginning of the experimental drop was very close to the extinction concentration (within 2%; see Fig. 3), uncertainty in the delay time was not a significant contributor to the uncertainty in the N₂ volume fraction. The expanded relative uncertainty in the N₂ volume fraction was 2%, dominated by uncertainty in the flows, based on a propagation of error analysis and repeat measurements. For all measurements reported here, the expanded uncertainty is presented with a coverage factor of 2, i.e., an uncertainty of 2 σ representing a 95% confidence interval.

The time for the flame to make the transition to microgravity was determined from observation of video images in experiments in which the N₂ concentration was held constant. The longest transition time, at 7 s⁻¹, was about 0.2 s, which was less than 10% of the total microgravity time available.

2.3. Temperature measurements

Measurement of the visible emission intensity from a 12.5 (± 0.5) μm β -SiC filament placed along the burner centerline allowed determination of flame temperatures for $T > 1200$ K. Below this temperature, the signal-to-noise ratio was inadequate. Radiation emitted by the filament was recorded using a digital CCD camera with a close-up lens such that the spatial resolution of the image was 0.07 mm/pixel. The camera exposure was adjusted to prevent image saturation (over-exposure) at the maximum flame temperature. Flame emission intensity was insignificant compared to filament intensity.

The total emissive power from a surface can be expressed using Planck’s Law integrated over all wavelengths as $E = \varepsilon\sigma T^4$. The fraction of the total radiance captured by the detector is a function of the spectral sensitivity of the detector, the transmissivity of the optics of the detector, and the solid angle. Because the spectral response curve of the detector and the transmissivity of the optics are not constant (and are unknown), a linear relationship between the detector signal and T^4 could not be assumed. A calibration

source was required to find the relationship between signal intensity and filament temperature.

The intensity measurements were calibrated using the one-dimensional OPPDIF flame code [9], following Ravikrishna and Laurendeau [14]. In order to equate the fiber luminescence to a fiber temperature, the profiles of the flame temperature and the emitted intensity along the length of the fiber for a given set of flame conditions was required. The correlation was based on a comparison of centerline counterflow flame measurements with OPPDIF calculations for a microgravity moderately strained methane–air diffusion flame with a N₂ concentration of 81% by volume in the fuel stream. The OPPDIF-predicted gas temperature profile was corrected to the predicted fiber temperature based on heat transfer to the fiber. The fiber temperature was then compared to the measured fiber luminosity and a correlation was determined with luminosity taken as proportional to the fiber temperature to the fifth power. The expanded uncertainty in the temperature measurement was typically 60 K, based on repeat measurements.

Because the conductivity along the filament is negligible [15], the energy balance becomes

$$hP(T - T_f) = \sigma\varepsilon PT_f^4, \quad (2)$$

where h is the convection coefficient, T is the gas temperature, T_f is the filament temperature, P is the perimeter of the filament, σ is the Stefan–Boltzmann constant, and ε is the filament emissivity. From solving Eq. (2) for T , a radiative correction for the gas temperature results:

$$T = T_f + \sigma\varepsilon T_f^4/h. \quad (3)$$

The convection coefficient was found by using a numerical correlation for low-velocity cross flow over a cylinder [16]. Experiments compared the filament intensity with the filament oriented horizontally and vertically in the counterflow flame to determine if there was a significant difference caused by filament orientation. The difference between the two orientations was 15 K, which was within experimental error, so the cross-flow assumption for the convection coefficient was considered acceptable. Extinction measurements, performed with and without the filament present, showed that the filament had a negligible effect (<0.1% difference) on the agent concentration required for extinction. Using an optical microscope, inspection of the filament after flame exposure revealed that there was no observable change in the diameter or other degradation in these relatively low-temperature short-duration experiments.

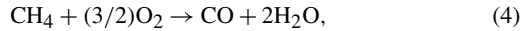
3. Numerical methods

The present computation employed a time-dependent axisymmetric configuration to treat counterflow diffusion flames formed between two opposed circular ducts. A coupled set of model-free equations with a low-Mach-number approximation was used following Ref. [17]. QUICK [18] and second-order central difference schemes were used to discretize the convective and diffusive terms. A predictor–corrector scheme nearly identical to that of Najm and Wyckoff [19] was used for time integration of the governing equations. Efficient algebraic relaxation for the velocity–pressure correction was performed using the HSMAC method [20]. CHEMKIN-II [21] and TRANFIT [22] were adopted for calculation of thermodynamic and transport properties. The computational domain in the axial direction was taken to be 40 mm. In the radial direction, domains of 70 and 50 mm were used for the zero- and normal-gravity conditions, respectively. In addition, 268×70 grids were used for the zero-gravity simulation and 268×65 grids for normal gravity. A uniform grid spacing of 0.15 mm was used in the axial direction. Radially, nonuniform grids with a minimum spacing of 0.3 mm were clustered near the centerline. A grid sensitivity study confirmed that the calculated extinction limit and the temperature maximum were unchanged when a finer grid (0.10 mm in the axial direction) was used, indicating that the heat release rate zone was adequately resolved.

The inflow temperature boundary condition for the reactant streams was 298 K. Uniform axial velocity was imposed at the mesh screens, which were positioned about 1.2 mm into each of the ducts. This condition is appropriate for global strain rates in 0g and 1g above about 7 and 15 s^{-1} , respectively, as exemplified by the temperature gradient, which is nominally flat under those conditions. Sides A and B shown in Fig. 2 were treated as outflow boundary conditions for the normal gravity and zero gravity calculations, respectively. A no-slip condition was applied on the burner walls and the wall temperature was taken as 298 K. A no-mass-flux condition was applied at all boundaries. The oxidizer stream was composed of undiluted air composed of 21% oxygen and 79% nitrogen by volume, and the fuel was methane diluted by nitrogen. The ambient gas was set to pure nitrogen, as in the experiment, to prevent secondary combustion of fuel.

A three-step irreversible reaction mechanism [23] for methane oxidation was used. Use of a larger, more comprehensive chemical mechanism was precluded due to practical reasons associated with computational cost. The three-step chemical model is adequate, as this paper focuses on the energetics associ-

ated with flame suppression, and not detailed reaction pathways. The detailed mechanism and reaction rates were taken as [23]



$$-d[\text{CH}_4]/dt = 10^{11.68} \times \exp(-23,500/T)[\text{CH}_4]^{0.7}[\text{O}_2]^{0.8}, \quad (7)$$

$$-d[\text{CO}]/dt = 10^{12.35} \times \exp(-19,200/T)[\text{CO}]^{1.0}[\text{H}_2\text{O}]^{0.5}[\text{O}_2]^{0.25}, \quad (8)$$

$$-d[\text{CO}_2]/dt = 10^{12.50} \times \exp(-20,500/T)[\text{CO}]^{1.0}[\text{H}_2\text{O}]^{0.5}[\text{O}_2]^{0.25}, \quad (9)$$

with reactions rates in $\text{kmol m}^{-3} \text{s}^{-1}$.

The viability of the three-step global mechanism was demonstrated by performing low-strain-rate flame calculations using OPPDIF and by comparing the calculations to flame measurements (see the discussion of Figs. 5 and 7 below). OPPDIF calculations using the GRI-3.0 mechanism [24] yielded agent extinction requirements very similar to those for OPPDIF calculations using the three-step mechanism, while the temperature peak using the three-step mechanism was less than 100 K larger than that obtained using GRI-3.0. Although detailed chemical reactions are not included in the three-step mechanism, it was considered appropriate to predict the extinction limits of N_2 -diluted methane flames, because nitrogen is known to extinguish a flame mainly by physical influences, such as heat capacity and dilution effects, rather than through chemical effects. An optically thin radiation submodel [25] was implemented, which considered heat loss from CH_4 , CO_2 , H_2O , and CO . Soot was not considered in these thin blue flames (see Fig. 4). The volumetric rate of radiative heat loss in the energy equation can be written as

$$\dot{q}_r = -4\sigma K_p(T^4 - T_\infty^4), \quad (10)$$

where T and T_∞ are the local and the ambient temperature, respectively. K_p is the Planck mean absorption coefficient of the mixture, which is expressed as

$$K_p = P_{\text{CH}_4}K_{\text{CH}_4} + P_{\text{CO}_2}K_{\text{CO}_2} + P_{\text{H}_2\text{O}}K_{\text{H}_2\text{O}} + P_{\text{CO}}K_{\text{CO}}, \quad (11)$$

where P_i and K_i denote the partial pressure and Planck mean absorption coefficient of species i , respectively, with K_p taken from Ref. [25].

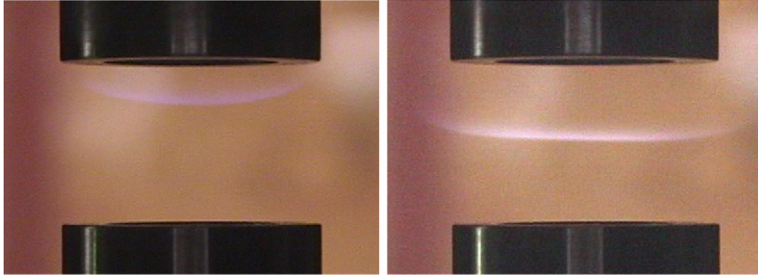


Fig. 4. Flames in normal gravity (left) and microgravity for $a_g = 20 \text{ s}^{-1}$ and a fuel stream (bottom duct) N_2 volume fraction of 0.80.

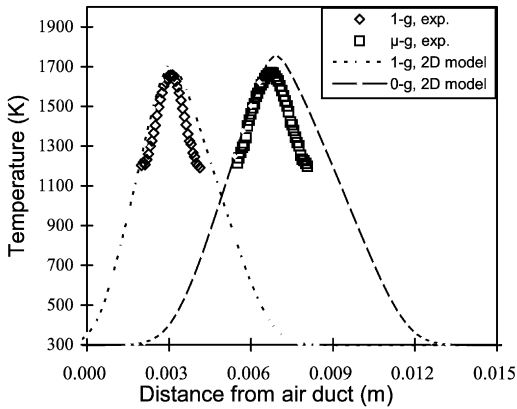


Fig. 5. Computed (2D model) and measured temperature profiles in normal gravity and microgravity for 20 s^{-1} methane–air flames with 0.80 N_2 volume fraction in the fuel stream. The expanded uncertainty in the temperature measurement was estimated as 60 K.

4. Results and discussion

Temperature profiles were measured along the burner axis and comparisons were made between the microgravity and normal gravity results. As the flame transitioned into microgravity, the maximum flame temperature location shifted towards the center of the flowfield and the flame width increased. Fig. 5 compares the measured axial temperature profiles in normal and microgravity for $a_g = 20 \text{ s}^{-1}$ and an N_2 volume fraction in the fuel stream equal to 0.80. The measured microgravity peak temperature was essentially the same as in normal gravity. The predicted (2D model) peak temperatures in the $0g$ and $1g$ flames were in agreement with the measured peaks to within experimental uncertainty (60 K), while the locations of the peaks were within about 0.3 mm of the measurements. The computed temperature fields are also shown in Fig. 6, which shows that the microgravity flame is thicker along the axis and over the entire flow field, consistent with the flame images seen in Fig. 4 and the calculated results shown in Fig. 5. The simulated flames appear to be similar

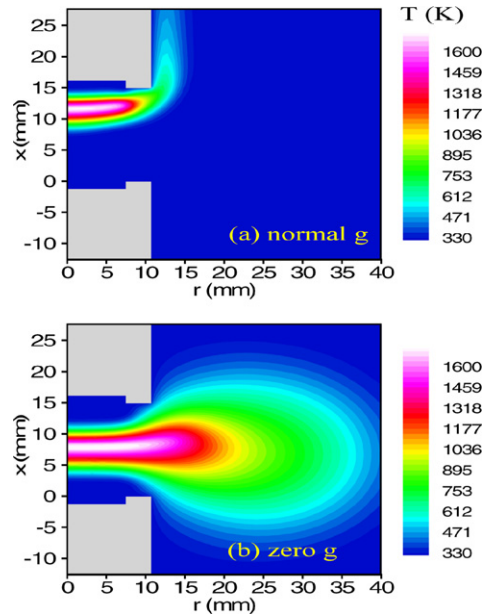


Fig. 6. Computed 2D temperature distributions of steady $a_g = 20 \text{ s}^{-1}$ near-suppression methane–air flames in (a) normal gravity and (b) zero gravity; compare to Fig. 4.

in shape to the experimentally observed visible flame shapes, but there is a tendency for the model to over-predict the fuel-side temperature. This is likely due to the limitations associated with the simplified global chemical model, which does not address real kinetic effects such as dissociation, recombination, and chain branching. Near the edge of the burner, even the microgravity flames are not simply one-dimensional in shape.

Fig. 7 shows measurements and one-dimensional (1D) and two-dimensional (2D) model calculations of the critical N_2 volume fraction in the fuel stream required to extinguish the methane–air diffusion flames as a function of the global strain rate. The figure compares the microgravity suppression measurements conducted here with the normal gravity results reported by Bundy et al. [2]. For the normal gravity flames, the air/fuel velocity ratio was adjusted so that

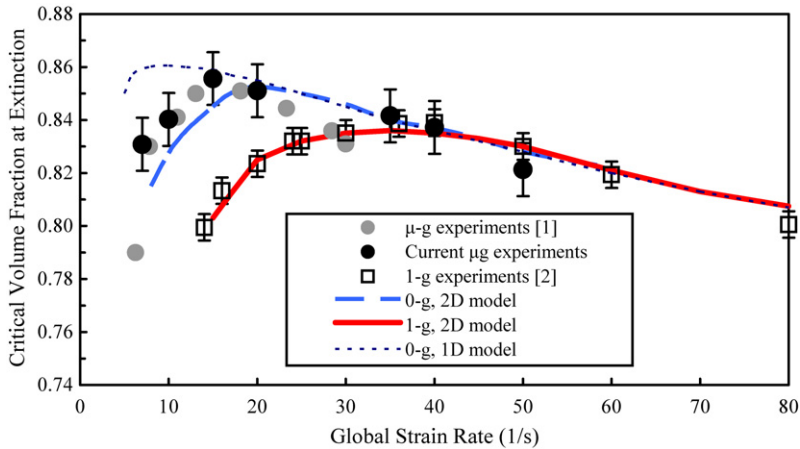


Fig. 7. Computed and measured critical nitrogen volume fraction in the fuel stream for suppression of CH_4 flames in microgravity and normal gravity.

the flame was positioned away from the burner duct, so that heat loss to the burner was negligible. The extinction data for normal gravity and microgravity collapse into one curve for moderate global strain rates ($a_g > 40 \text{ s}^{-1}$) as convective forces begin to dominate the effects of buoyancy. Fig. 7 also shows the microgravity suppression measurements of Maruta et al. [1], which are in agreement with the microgravity results presented here. The one-dimensional (1D) calculations of flame extinction (reported in [1] and confirmed in this study) failed to quantitatively reproduce the experimentally determined microgravity extinction results determined here and in Ref. [1] (see Fig. 1). This is attributed to the importance of lateral heat losses associated with radial conduction in the energy equation, which are neglected in the 1D similarity solution, but are considered in the 2D model calculation. The 2D modeling results shown in Fig. 7 appear to be adequate, showing agreement with the microgravity experiments to within experimental uncertainty, despite the use of simplified chemistry and radiation submodels. For the very lowest strain rates (10 s^{-1}), the 2D model somewhat underpredicts the critical agent concentration, due perhaps to the use of the optically thin radiation submodel, which tends to overpredict radiative heat loss, especially in the relatively thick lower strain rate flames.

The N_2 volume fraction in the fuel stream at the turning point represents the minimum agent needed to assure suppression regardless of strain rate. Its value in microgravity was measured as 0.855 ± 0.016 at a global strain rate of $15 \pm 5 \text{ s}^{-1}$. This value was higher than the analogous value in 1g. Fig. 7 shows that the microgravity suppression measurements and the 2D model suppression results drop sharply for strain rates lower than the turning point. The “turning point” in normal gravity occurred at a higher global strain rate

than in microgravity for both the simulations and the measurements.

At low strain rates, the extinction process is very different in normal gravity and microgravity, due to differences in flame structure. In this regard, it is helpful to consider the specific maximum heat release rate per unit volume divided by the local strain rate (SMHRR), which represents the flame strength along a flame surface as introduced by Sung et al. [26]. Calculations show that there is no effective difference between using the peak and the integrated reaction rates in comparing flame strength. Smaller values of SMHRR imply that the flame is weak and easier to extinguish. Table 1 compares the flame strength at three

Table 1

The computed (2D) local maximum heat release rate (HRR_{max}), the local strain rate (a_l), and the specific maximum heat release rate (SMHRR) as a function of radial location in 0g and 1g flames at $a_g = 10$ and 20 s^{-1} for an agent fuel stream volume fraction of 0.79

Location (r/R) ^a	HRR_{max} ($\text{J}/\text{cm}^3 \text{ s}$)	a_l (s^{-1})	SMHRR (J/cm^3)
0g; $a_g = 10 \text{ s}^{-1}$			
0.0	58.7	19	3.1
0.5	53.9	17	3.3
1.0	37.4	10	3.8
0g; $a_g = 20 \text{ s}^{-1}$			
0.0	110	36	3.1
0.5	107	33	3.2
1.0	82	19	4.3
1g; $a_g = 20 \text{ s}^{-1}$			
0.0	165	62	2.7
0.5	164	67	2.4
1.0	147	84	1.8

^a R is the inner duct radius; $r/R = 0$ is on the central axis.

locations for flames with global strain rates of 10 s^{-1} (0g) and 20 s^{-1} (0g and 1g) and an agent fuel stream volume fraction of 0.79. Table 1 lists the calculated (2D model) maximum heat release rate (HRR_{max}), the local strain rate (a_1), and the specific maximum heat release rate (SMHRR) as a function of radial location in the normal gravity and microgravity flames. The table shows that SMHRR at the center of the flow field is larger in the 0g 20 s^{-1} flame as compared to the 1g 20 s^{-1} flame. This is consistent with the results shown in Fig. 7 in which the normal gravity flame requires less agent to extinguish than the 0g flame, both at 20 s^{-1} . The calculated value of the SMHRR in 1g is nearly constant near the center of the flow field, but decreases by 1/3 of this value near the edge of the burner (at a radial distance, r , equal to the radius of the burner duct, R). This is consistent with the observation that the 1g low-strain-rate flame extinguishes from the outer edge first. The SMHRR of the 0g flame is also constant near the center, but increases toward the flame edge. Unlike the 1g flame, the microgravity flame under these conditions abruptly and simultaneously extinguishes over the entire flame surface. For the same global strain rate (see Eq. (1)), the local strain rate along the flame axis in the 0g flame ($= 36 \text{ s}^{-1}$) is about one-half the value of the local strain rate in the normal gravity flame ($= 62 \text{ s}^{-1}$). In 1g, buoyancy tends to enhance the local strain rate as hot gases are “pulled” above the burner (see Fig. 6). The table also shows that the SMHRR value at the edge of the 0g flames is lower in the 10 s^{-1} flame than in the 20 s^{-1} flame (both in 0g). This is consistent with the results shown in Fig. 7 in which the 10 s^{-1} flame requires somewhat less agent to extinguish than the 20 s^{-1} flame (both at 0g).

Fig. 8 shows the 2D model results of the local fractional energy loss contributed by key terms in

the energy equation (and normalized by the heat release rate) along the flowfield centerline of 0g and 1g flames with 0.79 N_2 volume fraction in the fuel stream as a function of the global strain rate. The figure also shows the radiative loss fraction determined in this study using the 1D model. The calculations show that axial conduction and diffusion are by far the largest heat loss mechanisms. The 2D model results indicate that radiative heat transfer is a significant energy loss mechanism in the 0g flames, becoming larger as the strain rate decreases. Radiative heat loss is not negligible even at moderate strain rates in near-extinction 0g flames, nor is it zero in 1g flames. Radial diffusion is found to be a relatively small contributor to energy loss for global strain rates above about 20 s^{-1} in both the 0g and 1g flames. Its magnitude is about one-half that of the radiative loss term for a global strain rate of 10 s^{-1} in the 0g flames. The combination of these loss mechanisms becomes larger as the strain rate decreases below the turning point at 15 s^{-1} , consistent with the observed decrease in agent concentration requirements presented in Fig. 7. Fig. 8 shows that the radiative loss terms in the 2D and 1D models were similar in magnitude.

5. Summary and conclusions

A fundamental study of the structure and suppression of low-strain nonpremixed flames was conducted using experiments and numerical computations. For the first time, temperature profiles were determined in near-extinction diffusion flames in microgravity. The temperature profile measurements, along with measurements of the critical agent suppression requirements, were used to validate the 2D flame code. The

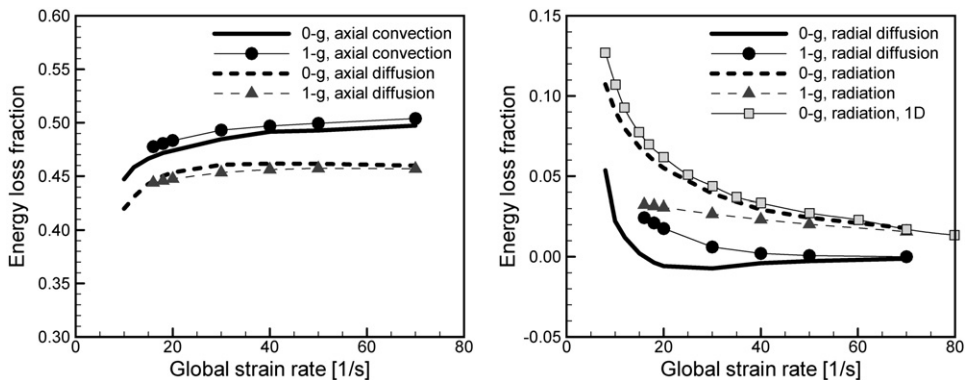


Fig. 8. Results of 2D model calculations of the fractional contribution by axial convection, axial diffusion, radial diffusion, and radiation in the energy equation (normalized by the heat release rate) in 0g (lines) and 1g flames (symbols) along the flow field centerline with 0.79 N_2 volume fraction in the fuel stream as a function of the global strain rate. The radiative loss fraction determined using the 1D calculation is also shown.

2D model calculations also showed agreement with experimental observation of flame curvature.

Analysis, using flame simulations, allows insight into the heat transfer processes that control flame structure and extinction. At low strain rates, the flames are rather thick and lateral heat and diffusion losses are not negligible. For finite-size burners, the simulations confirm that low-strain-rate counterflowing nonpremixed flames cannot be assumed to be purely one-dimensional in normal gravity or even microgravity. The commonly used one-dimensional flame codes do not provide a full picture of the multidimensional counterflow structure for experiments involving low-strain normal gravity or microgravity flames. By providing physical insight, two-dimensional simulations are a useful tool for guiding the interpretation of counterflow flame experiments.

Acknowledgments

This research was partially supported by the NASA Microgravity Research Division through Contract No. C-32066-T with Dr. Sandra Olson serving as Technical Monitor. The authors are grateful to Drs. K. Maruta, K.Y. Lee, J. Logue, W.C. Park, J. Park, and I.K. Puri for helpful discussions.

References

- [1] K. Maruta, M. Yoshida, H. Guo, Y. Ju, T. Niioka, *Combust. Flame* 112 (1998) 181–186.
- [2] M. Bundy, A. Hamins, K.Y. Lee, *Combust. Flame* 103 (2003) 299–306.
- [3] H. Zhang, F.N. Egolfopoulos, *Proc. Combust. Inst.* 28 (2000) 1875–1882.
- [4] P.D. Ronney, *Acta Astronaut.* 12 (1985) 915.
- [5] B.A. Van der Wege, M.T. Bush, S. Hochgreb, Effect of CF_3H and CF_3Br on laminar diffusion flame in normal and microgravity, in: *Proceedings of the Fourth International Microgravity Combustion Workshop*, NASA Conference Publication 10174, 1995, pp. 369–374.
- [6] J. Sutula, J. Jones, J.L. Torero, J. Borlik, O.A. Ezekoye, Diffusion flame extinction in low strain flow, in: *Proceedings of the Fourth International Microgravity Combustion Workshop*, NASA Conference Publication 10194, 1997, pp. 87–92.
- [7] F.A. Williams, Influences of water on methanol droplet burning and extinction, in: *Proceedings of the Fourth International Microgravity Combustion Workshop*, NASA Conference Publication 10174, 1997, pp. 449–454.
- [8] S.L. Olsen, J.S. T'ien, *Combust. Flame* 121 (2000) 439–452.
- [9] A. Lutz, R.J. Kee, J. Grcar, F.M. Rupley, A Fortran Program Computing Opposed Flow Diffusion Flames, SAND96-8243, Sandia National Laboratories, 1997.
- [10] C.E. Frouzakis, J. Lee, A.G. Tomboulides, K. Boulouchos, *Proc. Combust. Inst.* 27 (1998) 571–577.
- [11] K. Seshadri, F.A. Williams, *Int. J. Heat Mass Transfer* 21 (1978) 251.
- [12] B. Han, A.F. Ibarreta, C.J. Sung, J. T'ien, *Combust. Flame* 149 (2007) 173–190.
- [13] M. Kelly, NIST, Report of paramagnetic analyzer test results, personal communication, March 20, 2000.
- [14] R.V. Ravikrishna, N.M. Laurendeau, *Combust. Flame* 120 (2000) 372–382.
- [15] V. Vilimpc, L.P. Gross, *Proc. Combust. Inst.* 22 (1988) 1907–1914.
- [16] A. Zhukauskas, J. Ziugzda, *Heat Transfer of a Cylinder in Cross Flow*, Hemisphere Pub., New York, 1985.
- [17] C.B. Oh, C.E. Lee, J. Park, *Combust. Flame* 138 (2004) 225–241.
- [18] B.P. Leonard, *Comput. Methods Appl. Mech. Eng.* 19 (1979) 59–98.
- [19] H.N. Najm, P.S. Wyckoff, *Combust. Flame* 110 (1997) 92–112.
- [20] C.W. Hirt, J.L. Cook, *J. Comput. Phys.* 10 (1972) 324–340.
- [21] R.J. Kee, F.M. Rupley, J.A. Miller, CHEMKIN-II: A Fortran Chemical Kinetics Package for the Analysis of Gas Phase Chemical Kinetics, Report No. SAND89-8009B, Sandia National Laboratories, 1989.
- [22] R.J. Kee, G. Dixon-Lewis, J. Warnatz, M.E. Coltrin, J.A. Miller, A Fortran Computer Code Package for the Evaluation of Gas-Phase Multicomponent Transport Properties, Report No. SAND86-8246, Sandia National Laboratories, 1986.
- [23] F.L. Dwyer, I. Glassman, *Proc. Combust. Inst.* 14 (1972) 987–1003.
- [24] C.B. Oh, A. Hamins, M. Bundy, J. Park, *Combust. Theory Model.* (2006), submitted for publication.
- [25] Y. Ju, H. Guo, K. Maruta, F. Liu, *J. Fluid Mech.* 342 (1994) 315–334.
- [26] C.J. Sung, J.B. Liu, C.K. Law, *Combust. Flame* 102 (1995) 481–492.